

Electronic structure and thermodynamic stability of double-layered SrTiO₃(001) surfaces: *Ab initio* simulations

Eugene Heifets,¹ Sergei Piskunov,^{2,3,4,*} Eugene A. Kotomin,^{2,5} Yuri F. Zhukovskii,^{2,3} and Donald E. Ellis³¹California Institute of Technology, MS 139-74, Pasadena, California 91125, USA²Institute of Solid State Physics, University of Latvia, 8 Kengaraga Street, Riga LV-1063, Latvia³Department of Physics and Astronomy, Northwestern University, Evanston, Illinois 60208-3108, USA⁴Forschungszentrum Jülich, IWV-3, D-52425 Jülich, Germany⁵Institute for Transuranium Elements, European Commission Joint Research Center, D-76125 Karlsruhe, Germany

(Received 16 October 2006; revised manuscript received 18 January 2007; published 19 March 2007)

Using the B3PW hybrid exchange-correlation functional within density-functional theory and employing Gaussian-type basis sets, we calculated the atomic and electronic structures and thermodynamic stability of three double-layered (DL) SrTiO₃(001) surfaces: (i) SrO-terminated, (ii) TiO₂-terminated, and (iii) (2 × 1) reconstruction of TiO₂-terminated SrTiO₃(001) recently suggested by Erdman *et al.* [Nature (London) **419**, 55 (2002)]. A thermodynamic stability diagram obtained from first-principles calculations shows that regular TiO₂- and SrO-terminated surfaces are the most stable. The stability regions of (2 × 1) DL TiO₂- and DL SrO-terminated surfaces lie beyond the precipitation lines of SrO and TiO₂ compounds and thus are less stable with respect to regular SrTiO₃(001) surfaces. Analysis of the stability diagram suggests that Sr precipitation on SrTiO₃ surface never occurs. Our simulations show a substantial increase of Ti-O covalency on the DL surfaces as compared to the regular surfaces, which are themselves more covalent than the crystalline bulk. The implications of our calculated results for recent experimental observations are discussed.

DOI: 10.1103/PhysRevB.75.115417

PACS number(s): 68.35.Bs, 68.35.Md, 68.47.Gh

I. INTRODUCTION

SrTiO₃ perovskite is a technologically important material widely applied in catalysis and thin-film growth.^{1,2} Therefore, its surface properties are of high scientific interest. A large number of studies have been performed in recent years to understand and to determine a variety of SrTiO₃ surface structures realized under different experimental conditions.^{3–21} Some of the reported experimental observations are summarized in Table I.

At temperatures above 105 K, SrTiO₃ possesses a simple cubic perovskite symmetry with lattice constant of 3.905 Å (Ref. 22) and thus is an excellent model material for the whole ABO₃ perovskite group. Considering a SrTiO₃ formula unit with the formal charges of Sr²⁺, Ti⁴⁺, and O²⁻ ions, one can realize that the (001) surface is the most stable among other possible low index surfaces due to electrical neutrality of planes parallel to the surface.²³ There are two nonpolar (001) terminations of cubic SrTiO₃: SrO and TiO₂. Both can exist without substantial reconstruction. The previously calculated surface energies for both SrO- and TiO₂-terminated SrTiO₃(001) were found to be almost equal,^{24–26} implying that surfaces with both terminations can coexist. (In these computations, thermodynamic equilibrium was not assumed and surface energies were calculated, neglecting atom exchange between the surfaces and environment.) This prediction was also indirectly confirmed from experimental observations presented by Szot and Speier.⁸ Using atomic force microscopy (AFM), they found regular steps of two types on a thermally untreated SrTiO₃(001) surface; 40% of them possessed the heights of 1.9 Å (half unit cell), and for 50% this height reached 3.9 Å (full unit cell), which indicates the presence of both types of terminations.

Atomically flat surfaces are of high importance for technological purposes. For instance, the SrO-terminated surface

is preferable for obtaining perfect two-dimensional epitaxy of cuprate films used in oxide channel field-effect transistors,^{6,27} while the TiO₂-terminated surface was found to be appropriate for growth of TiO₂ nanoclusters.²⁰ Apart from this, the existence of differently terminated surface domains may result in different growth kinetics. A number of methods for preparation of sufficiently smooth surfaces terminated by a single atomic layer have been recently developed. Since SrO is a basic oxide and TiO₂ is an acidic oxide, the pH controlled buffered NH₄F-HF (BHF) etch solution has been proposed to selectively dissolve the SrO layer of SrTiO₃(001).³ This method was successfully used to prepare a surface predominantly terminated with TiO₂ atomic planes. SrO-terminated SrTiO₃(001) can be produced by evaporating Sr metal in a background O₂ atmosphere and further deposition of an SrO monolayer on the substrate.^{4,5} Another method is a cleaning of the SrTiO₃ surface in 1-propanol followed by oxygen annealing;²⁸ further, Schrott *et al.* reported a method to generate the SrO-terminated surface through ashing in O₂.⁶

The behavior of mechanochemically treated surfaces during annealing in an O₂ atmosphere or ultrahigh vacuum (UHV) is of considerable interest. Depending on experimental conditions (gas environment, pressure, temperature), SrTiO₃(001) surfaces can undergo a wide range of structural transformations, from various reconstructions to formation of nanostructures on the surface (see Table I and references therein). Many of these surface reconstructions are very likely thermodynamically unstable. The results published in numerous papers and models proposed there for the surface structures are sometimes contradictory. For more detailed reviews on surface reconstructions and island formation, see Refs. 15 and 19. Thus, despite substantial efforts undertaken for understanding of structure variations in thermally treated SrTiO₃(001) surfaces, uncertainties remain.

TABLE I. Observed SrTiO₃(001) structures and related experimental conditions.

Structure	Treatment	p_{O_2} (atm)	T (K)	t (min)	Technique
Sr rich					
SrO termination	BHF, ashing	1.3×10^{-4}	973–1023	60	AFM, MEIS, XPS ^a
Sr-related islands	BHF	4.9×10^{-12}	1273	20	STM ^b
SrO islands		0.26	1373	1440	AFM ^c
SrO islands		Ambient atmosphere	1573	7200	MIEEM, PEEM, MIES, UPS, XPS ^d
SrO islands		2.6×10^{-12}	1573	20	STM, AES ^e
Ti rich					
TiO ₂ termination		1	1273	600	AFM, RHEED, CAICISS ^f
TiO ₂ termination	BHF	4.9×10^{-12}	1073	100	STM ^b
(1 × 1) TiO ₂ termination	BHF	9.9×10^{-14}	873	30	STM, LEED ^g
(1 × 1) TiO ₂ termination	BHF	3.7×10^{-9}	983	60	UPS, RHEED, MEIS ^h
(2 × 1) DL TiO ₂ termination		Oxygen flow	1223–1303	30–300	TEM, DFT ^{i,j}
(2 × 1) TiO ₂ termination	BHF	9.9×10^{-14}	1073–1173	30	STM, LEED ^g
(2 × 2) TiO ₂ termination	BHF	1.3×10^{-11}	923–1003	60	UPS, RHEED, MEIS ^h
<i>c</i> (4 × 2) DL TiO ₂ termination		Oxygen flow	1103–1203	30–300	TEM, DFT ^{i,k}
<i>c</i> (4 × 2) TiO ₂ termination	BHF	9.9×10^{-14}	1473	15	STM, LEED ^g
<i>c</i> (4 × 4) TiO ₂ termination	BHF	9.9×10^{-14}	1373	20	STM, LEED ^g
<i>c</i> (6 × 2) TiO ₂ termination		Oxygen flow	1323–1373	30–300	TEM ^j
($\sqrt{5} \times \sqrt{5}$)R26.6° TiO ₂ termination		10^{-13}	1103	120	LEED, PES ^l
TiO islands	BHF	Oxygen flow	1273	180	AFM, GIXD, CTR ^m
TiO and Ti ₂ O formations		1.3×10^{-11}	1273	1440	AFM ^c
TiO islands		0.2×10^{-10}	1243	150	HRTEM ⁿ
TiO ₂ islands		10^{-14}	1148	1200	STM ^o
Ti ₂ O ₃ islands		9.9×10^{-12}	1273–1573	120	SEM, STM, AES, MIES, UPS, STS ^p

^aReference 6.^cReference 10.ⁱReference 14.^mReference 18.^bReference 7.^fReference 11.^jReference 15.ⁿReference 19.^cReference 8.^gReference 12.^kReference 16.^oReference 20.^dReference 9.^hReference 13.^lReference 17.^pReference 21.

Additional interpretation of experimentally observed surface structures and proposed models can be derived from first-principles calculations on the thermodynamic stability of reconstructed surfaces. A phase diagram can be plotted using calculated surface Gibbs free energies, indicating the range of stability conditions.²⁹ The most stable surface has the smallest excess (with respect to the bulk crystal) Gibbs free energy due to the surface creation. This concept was applied for the first time by Padilla and Vanderbilt to BaTiO₃ perovskite surfaces.³⁰ In this study, simple TiO₂ and BaO oxides were taken as external reservoirs and chemical potentials were limited by precipitation of these oxides at the perovskite surface. Noguera and co-workers^{31,32} applied a similar approach, but in their studies the area of free SrTiO₃ surface existence was restricted by precipitation on the surface of Sr and Ti metals or by loss of oxygen into the surrounding environment. In these studies, oxygen in the environment was characterized in terms of its chemical potential. Chemical potentials are not values which can be easily measured. Therefore, whenever it is possible, it is preferable to express the Gibbs free energies through experimentally ac-

cessible values. Thus, Reuter *et al.*³³ and Johnston *et al.*³⁴ (see also cited papers) developed an approach allowing expression of the surface excess Gibbs free energy through easily measurable temperature and oxygen gas partial pressure by combining calculated and experimental data. Johnston *et al.*³⁴ calculated surface free energies of regular, (2 × 1) TiO₂, (2 × 1) Ti₂O₃,¹² and (2 × 1) double-layered (DL) TiO₂ (Ref. 14) as a function of TiO₂ chemical potential, oxygen partial pressure, and temperature, in order to determine theoretically the most stable reconstruction of TiO₂-terminated SrTiO₃(001) surface. Examining stability diagrams, they found that the regular unreconstructed surface should be more stable under a wide range of conditions, while the (2 × 1) Ti₂O₃ surface¹² can be stable only under very low oxygen pressure. The absence of scanning tunneling microscopy (STM) images for regular surfaces was explained by the authors as due to the small corrugation of its calculated charge densities. The (2 × 1) DL TiO₂-terminated surface¹⁴ was found to be stable in the presence of a substantial amount of oxygen vacancies (usually created by annealing of SrTiO₃ surfaces in UHV), TiO₂-rich environment, and

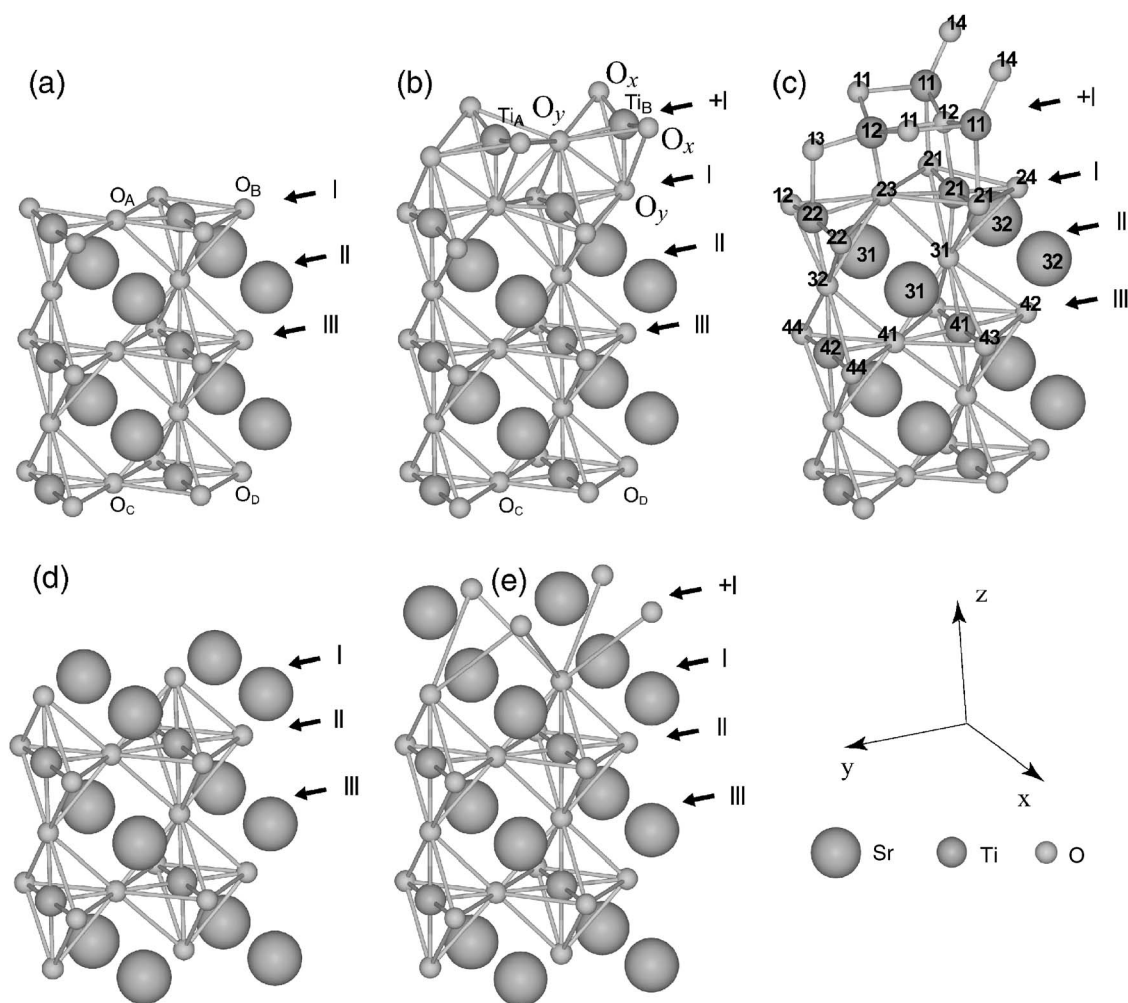


FIG. 1. Schematic view of the $\text{SrTiO}_3(001)$ surface structures considered: (a) regular TiO_2 termination, (b) DL TiO_2 termination, (c) (2×1) DL TiO_2 termination, (d) regular SrO termination, and (e) DL SrO termination. +I, I, II, and III enumerate the topmost slab layers, atoms of which were allowed to relax. Atomic labels accompanied with capital letters A, B, C, and D in (a) and (b) panels point out the corner atoms in Figs. 2(a) and 2(b). In order to make unreconstructed surfaces easily comparable with (2×1) $\text{SiTiO}_3(001)$, their surface unit cells are doubled in the y direction.

oxygen pressure greater than 10^{-8} atm. Liborio *et al.*³⁵ investigated the Sr-adatom model recently proposed by Kubo and Nozoye.⁷ This model consists of ordered Sr adatoms at the oxygen fourfold sites of a TiO_2 -terminated layer. Kubo and Nozoye applied the Sr-adatom model to explain almost all observed reconstructions of $\text{SrTiO}_3(001)$. Although the Sr-adatom model seems to be in contradiction with other models proposed [e.g., Erdman *et al.*^{14,16} explained SrO -deficient surface structures by removing alternate rows of oxygen from the TiO_2 -terminated surface to create (2×1) reconstruction], the calculated diagrams of thermodynamic stability confirmed that surface structures containing Sr-adatom coverages can be stable only when the surfaces are close to equilibrium with SrO oxide.³⁵

The main goal of this paper is to provide a deeper insight into the electronic structure and thermodynamic stability of DL $\text{SrTiO}_3(011)$ surfaces. This study is stimulated by Erdman *et al.* who, combining transmission electron microscopy (TEM) and direct method analysis, observed stable (2×1) and $c(4 \times 2)$ reconstructions of TiO_2 -terminated

$\text{SrTiO}_3(001)$.^{14–16} Applying periodic slab model and density-functional theory (DFT), the authors proposed a model which describes the observed surface reconstructions. Both surfaces were explained by the presence of an additional TiO_2 layer on the TiO_2 -terminated surface accompanied by consequent creation of oxygen vacancies^{14,16} [see Fig. 1(c) for (2×1) $\text{SrTiO}_3(001)$]. Apart from this, it was claimed that the regular unreconstructed TiO_2 -terminated surface is extremely unstable at high temperatures with respect to reconstruction. SrO was preferentially evaporated from the surface at the temperatures used in the experiment¹⁵ for annealing. In the present study, using the hybrid density-functional B3PW approach,³⁶ we calculated the electronic properties of $\text{SrTiO}_3(001)$ surfaces and their surface free energies as a function of oxygen and strontium chemical potentials. The oxygen chemical potential was then expressed in terms of oxygen gas partial pressure and temperature using known experimental data. We simulated the (2×1) DL TiO_2 -terminated surface suggested in Ref. 14 and compare it with DL and regular SrO - and TiO_2 -terminated $\text{SrTiO}_3(001)$

surfaces (see Fig. 1). DL unreconstructed surfaces contain an additional layer of SrO or TiO₂ for SrO- and TiO₂-terminated surfaces, respectively. The appearance of the second surface layer allows us to compare two possible modes of the oxide growth on the perovskite surface: through the layer-by-layer deposition and through formation of three-dimensional clusters. Thus, the calculated thermodynamic stability diagram could help us to decide which of the aforementioned methods of oxide growth is more feasible.

The outline of the paper is as follows. Section II describes the computational details of our calculations and surface structures considered; it also describes the thermodynamic approach we adopted to estimate the stability of surfaces. Section III contains the results obtained using calculations of electronic structures and thermodynamic stability of surfaces and their further discussion. Our conclusions are summarized in Sec. IV.

II. METHOD

A. Computational details

To perform hybrid B3PW calculations, we used the CRYSTAL computer code (see Ref. 37 and references therein), which employs Gaussian-type functions centered on atomic nuclei as the basis sets (BSs) for expansion of the crystalline orbitals. The BSs used in this study for SrTiO₃ surface and bulk computations were taken from Ref. 38: Sr, 311(1d)G; Ti, 411(311d)G; and O, 8-411(1d)G. The inner-core electrons of Sr and Ti atoms were described by small-core Hay-Wadt effective pseudopotentials.³⁹ The ability of the CRYSTAL code to treat both Hartree-Fock and Kohn-Sham equations on equal computational grounds allowed us to use the B3PW exchange-correlation functional³⁶ involving a “hybrid” of nonlocal Fock exact exchange, gradient-corrected [generalized gradient approximation (GGA)], and local (local-density approximation) exchange potentials combined with the GGA correlation potential of Perdew and Wang. This approach was successfully applied earlier for simulations on several regular and defective ABO₃ perovskites.^{26,38,40,41} The reciprocal space integration was performed by sampling the Brillouin zone with the 6×6 Pack-Monkhorst mesh⁴² for all surface structures under consideration. For bulk computations, we applied sampling with the 6×6×6 Pack-Monkhorst mesh. Such samplings provide balanced summation in direct and reciprocal lattices.

In this study, we consider SrTiO₃ in its high-symmetry cubic $Pm\bar{3}m$ phase. The optimized lattice constant³⁸ is 3.903 Å vs 3.905 Å observed in experiment.²² The lattice constant optimized by us for the bulk SrTiO₃ was used in the following simulations of surfaces.

Although the BSs mentioned above successfully described SrTiO₃, SrO, and TiO₂ oxides, they were found to be rather inadequate for Sr and Ti metals as well as for the oxygen molecule. Therefore, they had to be extended. We optimized additional diffuse Gaussian-type basis functions for metals [$\alpha_{sp}=0.0638$ (Sr), $\alpha_{sp}=0.1510$, and $\alpha_d=0.1317$ (Ti)]. This optimization was performed at experimental lattice constants. Then, lattice constants were reoptimized. For

Sr metal with $Fm\bar{3}m$ (fcc) structure, we obtained an optimized lattice constant $a_0=6.22$ Å (experiment yields 6.08 Å). Optimized lattice constants in Ti metal with $P6_3/mmc$ (hcp) structure (α -Ti) are $a_0=2.94$ Å and $b_0=4.69$ Å (experimental values are 2.95 and 4.68 Å, respectively). Single polarization d functions in oxygen BS were replaced by two d functions with exponents $\alpha_d=1.7271$ and $\alpha_d=0.6444$. As a result, we obtained an O₂ molecule bond length of 1.20 Å vs 1.21 Å in experiment. Calculated dissociation energy for the oxygen molecule (in triplet state) of 5.30 eV is in very good agreement with the experimental value of 5.12 eV. In the previous computations with gradient-corrected functionals,^{33,34,43} the oxygen dissociation energy was overestimated by 1 eV.

All optimizations of surface-atom positions were performed with the initial BS. Then, the extended BS was used to calculate total energies. The latter energies were used for calculation of surface Gibbs free energies and formation energies for SrTiO₃, SrO, and TiO₂. Our attempts to use the extended BS for optimizations of surface structures caused significant increase of computation time without significant change in simulation results. Therefore, we completed the analysis using the more economical procedure.

B. Surface structures

In the present study, we have calculated five surface structures: regular and DL SrO- and TiO₂-terminated and (2×1) DL TiO₂-terminated SrTiO₃(001) (see Fig. 1). Surface structures were modeled using a single two-dimensional (2D) slab model.²⁶ The equilibrium geometry was obtained using the conjugate gradient optimization procedure based on analytical computation of gradients, which is implemented in the CRYSTAL code.³⁷ Symmetrical (with respect to the middle plane) nine-layer slabs were adopted to simulate regular SrO- and TiO₂-terminated surfaces [Figs. 1(a) and 1(d), respectively]. In order to simulate DL SrO- and TiO₂-terminated surfaces [Figs. 1(b) and 1(e), respectively], we used 11-layer symmetrical slabs. Atoms in the additional top layer were placed in such a way that an appropriate cation-anion bonding was achieved. The DL (2×1) TiO₂-terminated SrTiO₃(001) surface is thoroughly described in Ref. 14. It demands a slab unit cell doubled in the y direction followed by creation of oxygen vacancies. This surface structure was modeled by us using an 11-layer slab as shown in Fig. 1(c).

Surface layers of all structures considered in our study consist of an integer number of either SrO or TiO₂ units.

C. Thermodynamic stability

The thermodynamic formalism adopted in the present study to estimate the stability of perovskite surfaces in equilibrium with matter reservoirs has been comprehensively described in Ref. 43 (see also references therein). The most stable surface composition and geometry is the one which minimizes the surface free energy. In this section, we summarize only the formulas required to calculate the surface free energy of the SrTiO₃(001) surface structures in equilibrium with surrounding oxygen atmosphere.

Bulk SrTiO_3 is assumed to be in equilibrium with the surface. Thus, the chemical potentials are mutually dependent through the Gibbs free energy of the bulk perovskite,

$$\mu_{\text{Sr}}(T,p) + \mu_{\text{Ti}}(T,p) + 3\mu_{\text{O}}(T,p) = \gamma_{\text{SrTiO}_3}^{\text{bulk}}(T,p), \quad (1)$$

where γ hereafter denotes Gibbs free energy per formula unit in a crystal. μ_{Ti} , μ_{Sr} , and μ_{O} are the chemical potentials of titanium, strontium, and oxygen, respectively.

Excesses (per surface unit cell area) of atoms A ($A=\text{O}$ or Sr) in the surfaces with respect to Ti atoms can be defined as

$$\Gamma_A^{\text{Ti}} = \frac{1}{2} \left(N_A^{\text{slab}} - N_{\text{Ti}}^{\text{slab}} \frac{N_A^{\text{bulk}}}{N_{\text{Ti}}^{\text{bulk}}} \right), \quad (2)$$

where N_i is the number of atoms i ($i=\text{Sr}$, Ti , and O) in slab or bulk unit cells. The factor $\frac{1}{2}$ appears since our surface system is modeled by a slab with two equivalent surfaces. Then, replacing the chemical potentials of Sr and Ti atoms by their deviations from chemical potentials in the most stable phases of respective elementary crystals,

$$\Delta\mu_{\text{Sr}}(T,p) = \mu_{\text{Sr}}(T,p) - \gamma_{\text{Sr}}^{\text{bulk}}, \quad (3)$$

$$\Delta\mu_{\text{Ti}}(T,p) = \mu_{\text{Ti}}(T,p) - \gamma_{\text{Ti}}^{\text{bulk}}, \quad (4)$$

and chemical potential of O atoms by its deviation from the energy of an oxygen atom in a free, isolated O_2 molecule ($E_{\text{O}_2}^{\text{total}}/2$),

$$\Delta\mu_{\text{O}}(T,p) = \mu_{\text{O}}(T,p) - \frac{E_{\text{O}_2}^{\text{total}}}{2}, \quad (5)$$

we can determine the surface Gibbs free energy from

$$\Omega = \phi - \Gamma_{\text{Sr}}^{\text{Ti}} \Delta\mu_{\text{Sr}} - \Gamma_{\text{O}}^{\text{Ti}} \Delta\mu_{\text{O}}, \quad (6)$$

where Ω is the energy per surface unit cell area, and ϕ is a constant defined below.

Gibbs free energies of SrTiO_3 bulk and slab can be approximated from first-principles calculations, evaluating their total energies. The vibrational contributions to surface Gibbs free energies are small and can be neglected in comparison with errors in electronic structure computations.³³ Therefore, it is possible to replace the slab and bulk Gibbs free energies by the corresponding total energies. Then we can express the constant ϕ in Eq. (6) as

$$\phi = \frac{1}{2} (E_{\text{slab}} - N_{\text{Ti}}^{\text{slab}} E_{\text{SrTiO}_3}^{\text{bulk}}) - \Gamma_{\text{Sr}}^{\text{Ti}} E_{\text{Sr}}^{\text{bulk}} - \Gamma_{\text{O}}^{\text{Ti}} \left(\frac{E_{\text{O}_2}}{2} \right), \quad (7)$$

where E_{slab} stands for total energy of a slab and replaces the Gibbs free energy of the slab.

In order to obtain the range of allowed values for μ_{Sr} and μ_{O} , we assume that Ti and Sr do not form a condensate on the surface. Consequently, the chemical potential of each species must be lower than the energy of an atom in the stable phase of the considered species:

$$\Delta\mu_{\text{Sr}}(T,p) < 0, \quad (8)$$

TABLE II. Calculated symmetry-allowed atomic displacements in percent of bulk lattice constant along the z direction for the regular and DL SrO- and TiO_2 -terminated $\text{SrTiO}_3(001)$. Negative sign means displacement toward the slab center. +I, I, II, and III enumerate slab layers, as shown in Fig. 1. For TiO_2 planes, O_x stands for the oxygen lying on the x axis, taking into account that the origin is placed on Ti atom [see Fig. 1(b)]. O_y stands for the oxygen on the y axis.

Layer	Atom	TiO ₂ termination		Atom	SrO termination	
		Regular	DL		Regular	DL
+I	Ti		6.98	Sr		11.73
	O _x		17.92	O		9.91
	O _y		0.12			
I	Ti	-2.45	0.56	Sr	-5.15	-3.65
	O _x	-0.27	-5.55	O	0.67	0.76
	O _y	-0.27	7.64			
II	Sr	3.59	-0.80	Ti	1.86	0.86
	O	0.38	-0.17	O _x	0.78	0.19
				O _y	0.78	0.19
III	Ti	-0.44	-0.09	Sr	-1.22	-0.53
	O _x	-0.05	-0.57	O	0.01	0.11
	O _y	-0.05	0.13			

$$\Delta\mu_{\text{Ti}}(T,p) < 0. \quad (9)$$

Equations (8) and (9) define the upper limits for the chemical potentials of Sr and Ti atoms. Introducing the Gibbs free energy of perovskite formation as follows:

$$\Delta G_{f_{\text{SrTiO}_3}}(T,p) = \gamma_{\text{SrTiO}_3}^{\text{bulk}}(T,p) - \gamma_{\text{Sr}}^{\text{bulk}}(T,p) - \gamma_{\text{Ti}}^{\text{bulk}}(T,p) - \frac{3}{2} \gamma_{\text{O}_2}^{\text{gas}}(T,p), \quad (10)$$

we can write down the lower limit for the deviation of oxygen chemical potential as follows:

$$\frac{1}{3} \Delta G_{f_{\text{SrTiO}_3}}(0,0) < \Delta\mu_{\text{O}}(T,p). \quad (11)$$

The formation energies of SrO and TiO_2 oxides are defined as

$$\Delta G_{f_{\text{SrO}}}(0,0) = \gamma_{\text{SrO}}^{\text{bulk}} - \gamma_{\text{Sr}}^{\text{bulk}} - \frac{E_{\text{O}_2}^{\text{total}}}{2} \quad (12)$$

and

$$\Delta G_{f_{\text{TiO}_2}}(0,0) = \gamma_{\text{TiO}_2}^{\text{bulk}} - \gamma_{\text{Ti}}^{\text{bulk}} - E_{\text{O}_2}^{\text{total}}, \quad (13)$$

respectively. Precipitation of the oxides does not occur if

$$\Delta\mu_{\text{Sr}}(T,p) + \Delta\mu_{\text{O}}(T,p) < \Delta G_{f_{\text{SrO}}}(0,0), \quad (14)$$

TABLE III. Atomic displacements calculated in this study (in percent of bulk lattice constant) for the (2×1) DL TiO_2 -terminated $\text{SrTiO}_3(001)$ are compared with those obtained in Refs. 14 and 34. Lattice constants used in Refs. 14 and 34 are 3.85 and 3.905 Å, respectively. For atom labels, see Fig. 1(c). Negative displacement along the z axis means displacement toward the slab center. Negative displacement along the y axis means displacement in the direction of left to right in Fig. 1(c). For conformity with data presented in Refs. 14 and 34, atom O_{41} is taken as a reference for the z position. Its displacement calculated in this study is $\Delta z = -1.89\%$ of a_0 . +I, I, II, and III enumerate slab layers, as shown in Fig. 1.

Layer	Atom	Δy			Δz		
		This study	Ref. 14	Ref. 34	This study	Ref. 14	Ref. 34
+I	Ti_{11}	-5.84	-7.04	-6.79	14.73	15.70	11.19
	Ti_{12}	4.28	4.10	3.33	6.09	10.19	8.22
	O_{11}	-5.58	-5.84	-6.66	19.16	23.61	19.77
	O_{12}	0.17	0.58	0.56	2.79	5.89	2.47
	O_{13}	-1.26	-0.92	-1.43	1.29	4.30	2.86
	O_{14}	22.77	14.04	13.74	49.93	45.89	42.25
I	Ti_{21}	-3.13	-2.92	-2.99	1.05	3.41	6.59
	Ti_{22}	3.19	2.80	2.74	2.97	5.99	4.53
	O_{21}	-3.34	-4.58	-4.78	5.80	10.19	7.31
	O_{22}	1.02	0.46	0.76	-2.88	-0.69	-1.12
	O_{23}	0.24	-0.14	-0.25	8.83	12.01	10.01
	O_{24}	0.24	0.02	0.08	-4.71	-3.20	-4.83
II	Sr_{31}	1.42	1.84	1.69	3.73	5.51	5.48
	Sr_{32}	-1.61	-1.94	-2.09	1.22	3.51	2.85
	O_{31}	4.99	6.18	6.67	3.80	6.30	4.97
	O_{32}	-3.74	-5.00	-5.17	1.02	2.89	2.98
III	Ti_{41}	0.21	0.42	0.39	1.58	3.00	3.52
	Ti_{42}	-0.99	-0.46	-0.65	2.39	4.20	4.40
	O_{41}	-0.11	-0.18	-0.10	0.00	0.00	0.00
	O_{42}	0.86	0.30	0.36	3.93	7.09	7.35
	O_{43}	0.27	0.00	0.04	2.74	4.99	5.22
	O_{44}	0.58	0.10	0.22	1.40	2.61	3.26

$$\Delta\mu_{\text{Ti}}(T,p) + 2\Delta\mu_{\text{O}}(T,p) < \Delta G_{f_{\text{TiO}_2}}(0,0). \quad (15)$$

Therefore, the region where SrTiO_3 surfaces are stable with respect to precipitation of Sr or Ti metals or their oxides is limited by the inequalities (8) and

$$\Delta G_{f_{\text{SrTiO}_3}}(0,0) < \Delta\mu_{\text{Sr}}(T,p) + 3\Delta\mu_{\text{O}}(T,p), \quad (16)$$

$$\begin{aligned} \Delta G_{f_{\text{SrTiO}_3}}(0,0) - \Delta G_{f_{\text{TiO}_2}}(0,0) &< \Delta\mu_{\text{Sr}}(T,p) + \Delta\mu_{\text{O}}(T,p) \\ &< \Delta G_{f_{\text{SrO}}}(0,0). \end{aligned} \quad (17)$$

At each value of $\Delta\mu_{\text{Sr}}$ and $\Delta\mu_{\text{O}}$, the most stable surface has the smallest surface Gibbs free energy defined by Eq. (6). If $\Omega(T,p)$ becomes negative, surface formation will lead to an energy gain. Then, the surface will form spontaneously and the crystal will disintegrate. Therefore, the condition of the crystal existence is that $\Omega(T,p)$ for all possible surfaces is positive.

Under experimental working conditions, both p_{O_2} and temperature are varied. Thus, it is most useful to consider the dependence of surface structure stabilities with respect to $\mu_{\text{O}}(T,p)$. The oxygen chemical potential should be determined by the condition of thermodynamic equilibrium with the surrounding O_2 gas phase reservoir. Thus, its temperature and pressure dependence is defined as

$$\mu_{\text{O}}(T,p) = \frac{1}{2} \left[E_{\text{O}_2}^{\text{total}} + \mu_{\text{O}_2}(T,p^0) + k_B T \ln \left(\frac{p}{p_0} \right) \right]. \quad (18)$$

The temperature dependence of $\mu_{\text{O}_2}(T,p^0)$ includes contributions from molecular vibrations and rotations, as well as ideal-gas entropy at 1 atm pressure. These data can be found in the thermodynamic tables.⁴⁴ Employing Eq. (18), one can obtain the oxygen chemical potential for any (T,p) pair and thus provide the diagrams of thermodynamic stability with clear physical meaning behind the calculated curves. The final relation reads (cf. Ref. 43)

TABLE IV. Calculated Mulliken effective charges Q (in e) and their deviations from bulk values ΔQ_{bulk} ($Q_{\text{Sr}}=1.87$, $Q_{\text{Ti}}=2.35$, and $Q_{\text{O}}=-1.41$) for the outermost layers of regular and DL SrO- and TiO₂-terminated SrTiO₃(001) (Fig. 1). For TiO₂ planes, O_x stands for the oxygen lying on the x axis, taking into account that the origin is placed on Ti atom [see Fig. 1(b)]. O_y stands for the oxygen on the y axis.

Layer	Atom	Regular		DL	
		Q	ΔQ_{bulk}	Q	ΔQ_{bulk}
TiO ₂ termination					
+I	Ti			2.29	-0.06
	O _x			-1.14	0.27
	O _y			-1.14	0.27
I	Ti	2.29	-0.06	2.31	-0.04
	O _x	-1.30	0.11	-1.26	0.15
	O _y	-1.30	0.11	-1.26	0.15
II	Sr	1.85	-0.02	1.86	-0.01
	O	-1.36	0.05	-1.44	-0.03
III	Ti	2.35	0.00	2.36	0.01
	O _x	-1.39	0.02	-1.41	0.00
	O _y	-1.39	0.02	-1.42	-0.01
SrO termination					
+I	Sr			1.84	-0.03
	O			-1.84	-0.43
I	Sr	1.84	-0.03	1.86	-0.01
	O	-1.52	-0.11	-1.60	-0.19
II	Ti	2.37	0.01	2.36	0.01
	O _x	-1.45	-0.04	-1.42	-0.01
	O _y	-1.45	-0.04	-1.42	-0.01
III	Sr	1.87	0.00	1.87	0.00
	O	-1.43	-0.02	-1.42	-0.01

$$\Delta\mu_{\text{O}}(T,p) = \frac{1}{2} \left[(H_{\text{O}_2}^{\text{gas}}(T,p^0) - H_{\text{O}_2}^{\text{gas}}(T^0,p^0) - TS_{\text{O}_2}^{\text{gas}}(T,p^0) + T^0 S_{\text{O}_2}^{\text{gas}}(T^0,p^0)) + k_B T \ln\left(\frac{p}{p^0}\right) \right] + \delta\mu_{\text{O}}^0, \quad (19)$$

where $T^0=298.15$ K and $H_{\text{O}_2}^{\text{gas}}$ and $S_{\text{O}_2}^{\text{gas}}$ are experimental enthalpy and entropy of gaseous oxygen, respectively. $\delta\mu_{\text{O}}^0$ denotes the correction, which should bring experimental data and results of quantum-mechanical computations in line (see Refs. 34 and 43 for details). This correction was estimated from calculated energies of a metal M , its oxide $M_x\text{O}_y$, and experimental data for oxygen gas entropy $S_{\text{O}_2}^{\text{gas}}(T^0,p^0)$ and formation enthalpy $\Delta H_{f,M_x\text{O}_y}^0$ for the metal oxide at the same standard conditions (T^0,p^0) using

TABLE V. The same as in the Table IV for the (2×1) DL TiO₂-terminated SrTiO₃(001) [see atom labels in Fig. 1(c)].

Layer	Atom	Q	ΔQ_{bulk}
+I	Ti ₁₁	2.16	-0.19
	Ti ₁₂	2.26	-0.10
	O ₁₁	-1.26	0.15
	O ₁₂	-1.38	0.03
	O ₁₃	-0.96	0.45
	O ₁₄	-0.77	0.64
I	Ti ₂₁	2.32	-0.04
	Ti ₂₂	2.31	-0.05
	O ₂₁	-1.35	0.06
	O ₂₂	-1.29	0.12
	O ₂₃	-1.26	0.15
	O ₂₄	-1.22	0.19
II	Sr ₃₁	1.86	0.00
	Sr ₃₂	1.86	-0.01
	O ₃₁	-1.40	0.01
	O ₃₂	-1.42	-0.01
III	Ti ₄₁	2.35	0.00
	Ti ₄₂	2.35	0.00
	O ₄₁	-1.37	0.04
	O ₄₂	-1.43	-0.02
	O ₄₃	-1.40	0.01
	O ₄₄	-1.41	0.00

$$\delta\mu_{\text{O}}^0 = \frac{1}{y} (h_{M_x\text{O}_y}^0 - x h_M^0 - \Delta H_{f,M_x\text{O}_y}) - \frac{1}{2} (E_{\text{O}_2}^{\text{total}} + T^0 S_{\text{O}_2}^{\text{gas}}(T^0,p^0)). \quad (20)$$

Here, the enthalpies for the metal h_M^0 and the metal oxide $h_{M_x\text{O}_y}^0$ can be replaced by calculated total energies because the pV term in the enthalpies is negligible. In this study, $\delta\mu_{\text{O}}^0$ was calculated for SrO (-0.389 eV) and TiO₂ (-0.361 eV). The variation between two values calculated here with the hybrid B3PW functional is only 0.028 eV. The uncertainty previously obtained with DFT is about 0.2 eV.^{34,43} Our present computations employing the hybrid functional produced a much more consistent correction for the oxygen chemical potential. This translates into significant improvement of precision in determination of the phase diagram for SrTiO₃ surfaces. For instance, for $T=1000$ K, uncertainty in determination of oxygen partial pressure decreases from 1000%-2000% for DFT to 40% for computations performed with the hybrid B3PW functional. These estimates are obtained by substitution of the above-mentioned uncertainties to Eq. (19).

III. RESULTS AND DISCUSSION

A. Atomic and electronic structures

For regular and DL TiO₂- and SrO-terminated surfaces, atoms in outermost slab layers were relaxed along directions

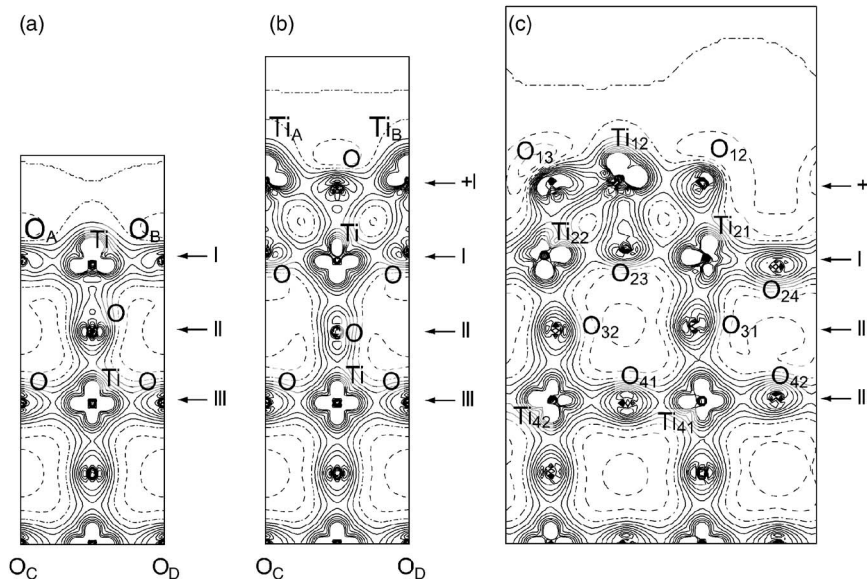


FIG. 2. 2D difference electron density maps with respect to the superposition of densities of Sr^{2+} , Ti^{4+} , and O^{2-} ions. Dot-dashed isolines correspond to the zero density level. Dashed isolines stand for a decrease in charge density (lack of electrons) and solid lines for an increase (excess of electron density). Isodensity curves are drawn from -0.05 to $+0.05$ $e \text{ a.u.}^{-3}$ with an increment of 0.05 $e \text{ a.u.}^{-3}$. (a) Regular TiO_2 termination, (b) DL TiO_2 termination, and (c) (2×1) DL TiO_2 termination. Atomic labels are shown according to Fig. 1.

allowed by symmetry (z axis). Their calculated displacements are listed in Table II. Atomic displacements for (2×1) DL TiO_2 -terminated $\text{SrTiO}_3(001)$ calculated in this study [Fig. 1(c)] were compared with those obtained in Refs. 14 and 34 (Table III). All three equilibrium geometries mentioned for this (2×1) reconstruction are in good agreement.

Due to the partly covalent nature of the Ti-O bond, the effective Mulliken charges of Ti and O atoms in SrTiO_3 bulk are far from formal ionic charges.³⁸ On the contrary, charge of the Sr atom ($1.87e$) is relatively close to its formal charge ($2e$). It is also known that Ti-O bond covalency increases in

$\text{SrTiO}_3(001)$ surface layers.²⁶ The calculated effective Mulliken charges and their deviations from the bulk values for regular and DL surfaces studied here are listed in Tables IV and V. The atomic charges of central unrelaxed layers of all surface structures do not change as compared to bulk. Significant changes of Mulliken charges are localized within two near-surface layers. In regular SrO- and TiO_2 -terminated surfaces, change of the total charge density on two surface layers is approximately equal to half of the charge density on $[001]$ planes in the bulk of SrTiO_3 crystal. In DL TiO_2 and SrO terminations, additional layers stay neutral. Charge den-

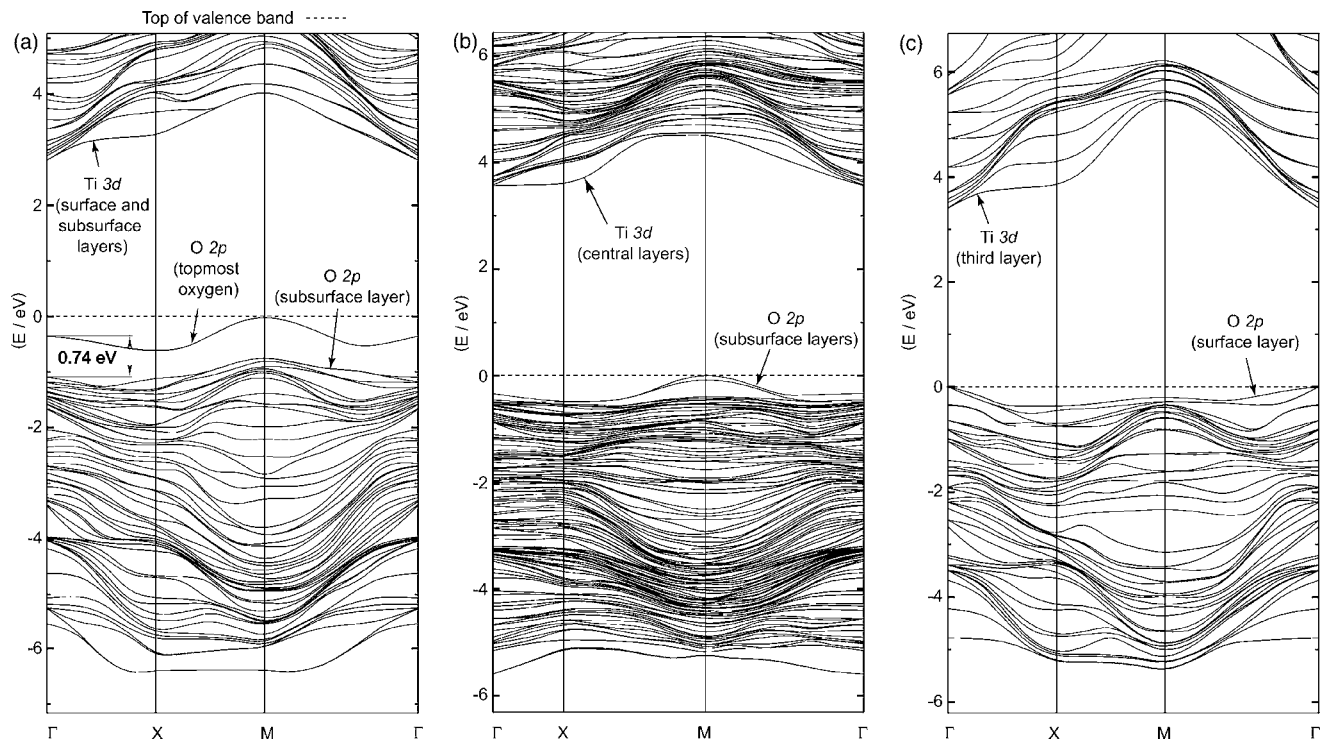


FIG. 3. Calculated band structures for $\text{SrTiO}_3(001)$: (a) DL TiO_2 -terminated, (b) (2×1) DL TiO_2 -terminated, and (c) DL SrO-terminated.

TABLE VI. Calculated optical band gaps (in eV) for all surface structures and bulk SrTiO₃.

Structure	Band gap
Regular TiO ₂ termination	2.66
DL TiO ₂ termination	2.80
(2 × 1) DL TiO ₂ termination	3.54
Regular SrO termination	3.67
DL SrO termination	3.40
Bulk SrTiO ₃	3.63
Expt. ^a	3.25

^aReference 46.

sity in the additional layer in the (2 × 1) DL TiO₂-terminated surface is positive and small. Charges of ions in all additional layers are noticeably different from charges in the SrTiO₃ bulk. The charge difference is especially large on O ions. Charge-density change in the subsurface layer (labeled as I in Fig. 1) in all DL-terminated surfaces appeared also to be close to half of the charge density on planes in the crystal bulk. In all TiO₂-terminated surfaces, charges of surface ions decreased, which suggests an increase in covalent contributions to bonding. The opposite change can be found in SrO-terminated surfaces: magnitude of charges on surface ions grows, indicating more ionic bonding in the surface layer.

Further evidence for the increase of Ti-O covalency is drawn from the differential electron density maps shown in Fig. 2. Solid isolines of excess electron density (as compared to formal ionic states) denote a formation of covalent bonding. The increase of difference electronic density in the proximity of surface atoms of DL TiO₂-terminated surfaces is clearly seen.

Band structures calculated for DL SrTiO₃ surfaces considered in this study are shown in Fig. 3. The valence band (VB) of all surfaces consists of O 2*p* orbitals with small admixture of Ti 3*d* states at the VB bottom that gives a hybridization between these states, explaining the nature of partial Ti-O covalency. The VB top for all surface structures is mainly formed by 2*p* orbitals of surface O (the only exception is the regular SrO-terminated surface, in which the VB top is formed by 2*p* orbitals of oxygen from the slab center). The bottom of the conduction band is mainly formed by Ti 3*d* levels. The 2*p* level of the outermost oxygen in the

TABLE VII. Excesses [Eq. (2)] of O and Sr atoms in the surfaces with respect to Ti atoms and free energy of formation [Eq. (7)] for SrTiO₃(001) surfaces under consideration.

Surface	$\Gamma_{\text{O}}^{\text{Ti}}$	$\Gamma_{\text{Sr}}^{\text{Ti}}$	ϕ (eV/unit cell)	ϕ (J/m ²)
Regular TiO ₂	$-\frac{1}{2}$	$-\frac{1}{2}$	4.84	5.06
DL TiO ₂	$-\frac{3}{2}$	$-\frac{3}{2}$	13.07	13.65
(2 × 1) DL TiO ₂	-3	-3	25.14	13.12
Regular SrO	$\frac{1}{2}$	$\frac{1}{2}$	-2.63	-2.75
DL SrO	$\frac{3}{2}$	$\frac{3}{2}$	-8.49	-8.86

TABLE VIII. Calculated Gibbs free formation energies ΔG_f (eV) for bulk SrO and TiO₂ oxides and SrTiO₃ perovskite. Last column contains experimental data (Ref. 45) [in the limit of low temperature $\Delta G_f(T \rightarrow 0 \text{ K}, 1 \text{ atm})$].

Crystal	Calc. ΔG_f	Expt. ΔG_f
SrTiO ₃	-17.29	-17.31
TiO ₂	-9.78	-9.77
SrO	-6.16	-6.11

band structure of the (1 × 1) DL TiO₂-terminated surface is of particular interest [Fig. 3(b)]. This level is split completely from the VB (by 0.74 eV in Γ and M points and by 0.35 eV in X point). Calculated band gaps E_g are summarized in Table VI. DL SrO-terminated SrTiO₃(001) exhibits a direct Γ - Γ gap, while other surface structures and bulk SrTiO₃ possess an indirect M - Γ gap. The bulk SrTiO₃ also has an indirect E_g , but the top of the valence band is located at the R k point. The DL TiO₂-terminated surfaces yield increased E_g as compared to a regular TiO₂-terminated surface. Band gaps in all TiO₂-terminated surfaces are significantly smaller than the bulk E_g . The band gap in DL SrO-terminated surface is 0.2 eV smaller than E_g in bulk SrTiO₃, while that of the regular SrO-terminated surface is just slightly (by 0.05 eV) wider than the bulk value. It is worth mentioning here that hybrid exchange-correlation functionals are claimed to provide most reliable band gaps for perovskite materials.³⁸

B. Surface stability

The present *ab initio* simulations allowed us to determine all parameters needed to calculate surface free energies [Eq. (6)] for a variety of surfaces (Table VII) and formation energies (Table VIII) for crystalline SrTiO₃, SrO, and TiO₂. These data were used to calculate positions of boundaries between stability regions for different surface terminations. The boundary between stability regions for surfaces with terminations A and B is determined from the equation

$$\Omega^A = \Omega^B. \quad (21)$$

In all relevant cases, the solution of this equation can be written as

$$\Delta\mu_{\text{Sr}} + \Delta\mu_{\text{O}} = g_{AB}, \quad (22)$$

where values g_{AB} are collected in Table IX.

TABLE IX. Positions of boundaries g_{AB} (eV) [Eq. (22)] between stability regions of surfaces with terminations A and B shown in phase diagram (Fig. 4).

Termination A	Termination B	g_{AB}
DL TiO ₂	(2 × 1) DL TiO ₂	-8.05
Regular TiO ₂	(2 × 1) DL TiO ₂	-8.12
Regular TiO ₂	Regular SrO	-7.47
Regular SrO	DL SrO	-5.86

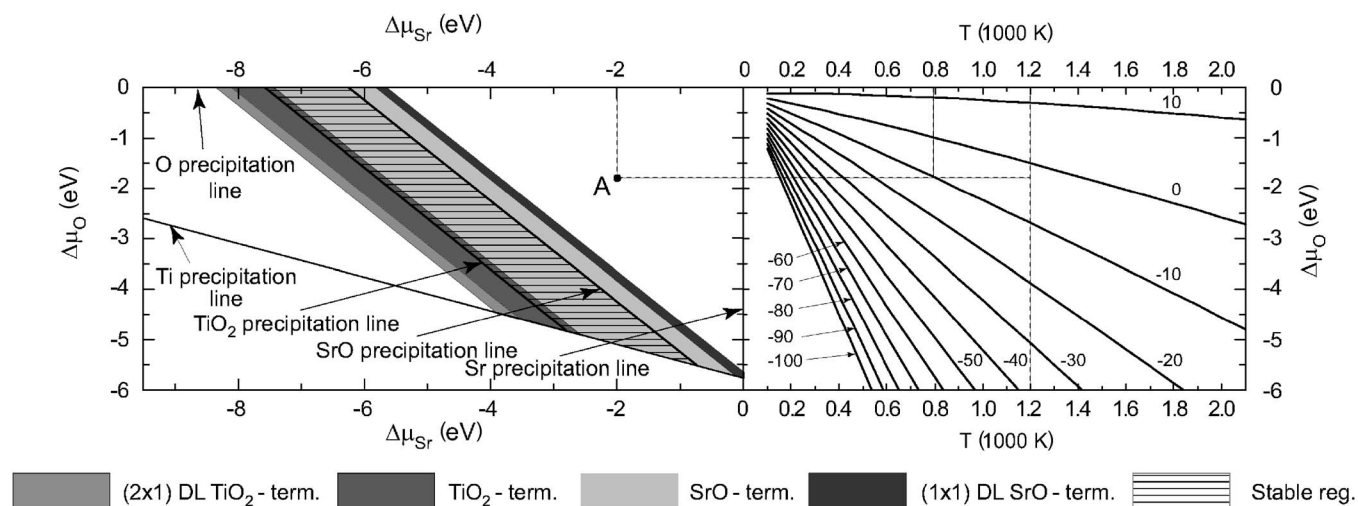


FIG. 4. Phase diagram: the regions of stability of SrTiO_3 surfaces with different terminations [TiO_2 -, (2×1) DL TiO_2 -, SrO -, and (1×1) DL SrO -terminated (001) surfaces] as function of chemical potential variations for strontium [Eq. (3)] and oxygen [Eq. (5)] atoms. Parameters for all lines on the left side of the figures are collected in Tables VII–IX. The right side of the figures contains a family of $\Delta\mu_{\text{O}}$ as functions of temperature at various oxygen gas pressures according to Eq. (19). The labels m on the lines represent the pressure $p_{\text{O}_2} = 10^m$ atm.

Our attention was attracted by unexpectedly good agreement of calculated energies of formation with experimental data. Consistency of calculated and experimental values⁴⁵ is nearly perfect. Such good agreement may be attributed to the hybrid functional employed in our simulations. In the previous DFT computations, the error in formation energies was as large as 1 eV.^{34,43}

The calculated stability diagram is presented in Fig. 4. It shows regions of oxygen and strontium chemical potentials, where surface free energies [Eq. (6)] calculated for different terminations are minimal. The O-poor limit defined by Eq. (11) is 5.7 eV. The Sr-rich limit [Eq. (8)] is $\Delta\mu_{\text{Sr}} = 0$ eV; at this limit, precipitation of strontium occurs. The border, at which precipitation of Ti at surfaces will be observed, is defined by Eq. (16), and precipitation of oxides is defined at limits set in Eq. (17). The precipitation lines in Fig. 4 limit the region of the SrTiO_3 stability. The areas beyond the shaded regions correspond to negative Gibbs free surface energies, meaning conditions under which a SrTiO_3 crystal disintegrates by spontaneous surface formation. The SrTiO_3 bulk and surfaces are presumed to be in equilibrium with surrounding oxygen gas atmosphere.

To illustrate behavior of surface energies for the $\text{SrTiO}_3(001)$ surface structures under consideration, we plotted Gibbs free energies for several special conditions. In all cases, temperature was set to 1000 K. The surface Gibbs free energies defined in Eq. (6) for oxygen gas pressure equal to 1 atm were plotted in Fig. 5. Figure 6(a) contains the surface Gibbs free energies along the TiO_2 precipitation line, and Fig. 6(b) presents them along the SrO precipitation line.

The right side of the stability diagram (Fig. 4) contains a set of curves, which show the dependencies of oxygen chemical potentials on temperature for a number of gas pressures according to Eq. (19). It can be used in the following way: let the system be, for example, at temperature of 1200 K and we are interested to know at what pressure oxy-

gen gas will be in equilibrium with the surface. To do this, we can draw a vertical line at $T = 1200$ K on the right side of the diagram. Crossings of the plotted functions with this line form a scale for gas pressure. Then, for any point A (Fig. 4), we can determine the equilibrium gas pressure. Similarly, if the gas is under any particular pressure (for example, at 10–20 atm), we should watch for the crossing point of a horizontal line, originating from point A, with the function for oxygen chemical potential corresponding to that pressure. Then projection of this crossing point on the temperature axis provides us with the equilibrium temperature.

The calculated stability diagram (Fig. 4) explicitly shows that the regular unreconstructed surfaces are the most stable. The largest stable region area belongs to the regular SrO -terminated surface. The region where a TiO_2 -terminated surface is stable is very narrow within the SrTiO_3 stability re-

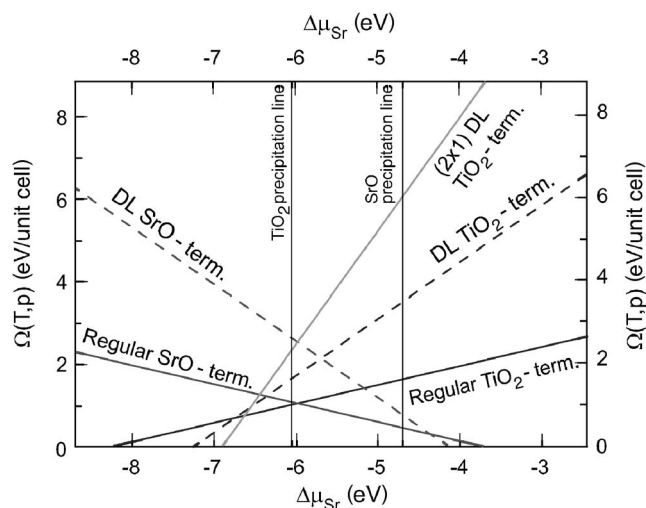


FIG. 5. Surface Gibbs free energies as a function of μ_{Sr} at $T = 1000$ K and $p_{\text{O}_2} = 1$ atm.

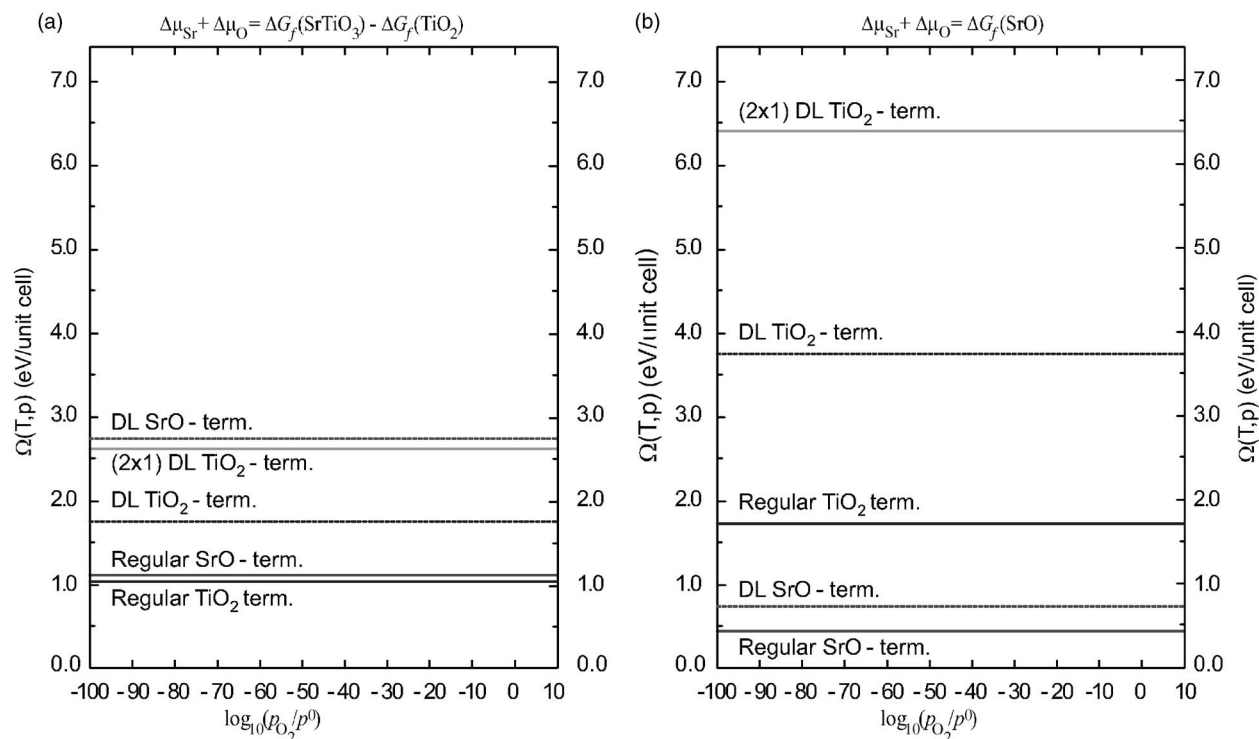


FIG. 6. Surface Gibbs free energies as a function of $\log_{10}(p_{\text{O}_2}/p^0)$ at $T=1000$ K for (a) $\Delta\mu_{\text{Sr}} + \Delta\mu_{\text{O}} = \Delta G_f(\text{SrTiO}_3) - \Delta G_f(\text{TiO}_2)$ (along the TiO_2 precipitation line) and (b) $\Delta\mu_{\text{Sr}} + \Delta\mu_{\text{O}} = \Delta G_f(\text{SrO})$ (along the SrO precipitation line).

gion and runs along the TiO_2 precipitation line. The regions of stable DL surfaces lie far beyond the region of SrTiO_3 crystal stability limited by oxide precipitation lines. This allows us to conclude that the formation of DL surface structures cannot be formed under equilibrium conditions. In other words, instead of layer-by-layer mode, oxides grow as islands and then as microcrystals. The experimental confirmation for this can be drawn from Table I. Kazimirov *et al.* reported the formation of monoclinic TiO crystallites¹⁸ at temperature and/or pressure conditions similar to those at which Erdman *et al.*¹⁴ observed (2×1) DL TiO_2 -terminated $\text{SrTiO}_3(001)$. However, Erdman *et al.* did not etch the sample by BHF. Note that Sr and SrO precipitation lines do not cross in the calculated stability diagram; moreover, the Sr precipitation line crosses only a very small region of stability of the DL SrO-terminated surface. This means that precipitation of metallic Sr at surfaces in equilibrium is rather impossible. If we start from any point within the SrTiO_3 stability region and decrease oxygen pressure while keeping temperature constant, then the only precipitation lines, which can be crossed, are TiO_2 and Ti precipitation lines. Similarly, if the Sr chemical potential will move toward the Sr-rich limit at constant temperature and oxygen gas pressure, then we will observe precipitation of SrO. There is no way to reach the Sr precipitation line from the SrTiO_3 stability region without crossing first some other precipitation line.

The calculated diagram of thermodynamic stability corresponds to equilibrium conditions and does not account for any kinetic processes. However, it is known that at high temperatures, oxygen vacancies are created at SrTiO_3 surfaces even in the presence of oxygen atmosphere.^{47,48} Newly formed vacancies diffuse into the bulk. Thus, it is most likely

that Ti atoms are more mobile with respect to heavy Sr atoms and tend to reorganize the surface under appropriate temperature and/or pressure conditions. Therefore, larger time is needed for formation of SrO islands due to agglomeration,⁹ while TiO_x islands disappear when annealing time is increased.¹⁹

IV. CONCLUSIONS

Using the B3PW hybrid exchange-correlation functional and thermodynamic analysis, we calculated the electronic properties and estimated thermodynamic stability of three DL $\text{SrTiO}_3(001)$ surfaces: SrO-, TiO_2 -, and (2×1) TiO_2 -terminated surfaces, as well as regular unreconstructed SrO- and TiO_2 -terminated $\text{SrTiO}_3(001)$.

We found that on all TiO_2 -terminated surfaces, covalency contributions to the Ti-O chemical bonding are increased compared to the bulk. On the contrary, bonding in SrO-terminated surfaces is slightly more ionic than in SrTiO_3 bulk. The highest valence bands in surfaces with DL terminations are formed by $2p$ functions of the surface oxygen ions. On an unreconstructed DL TiO_2 -terminated surface, the surface valence band is completely split from the rest of the valence bands, although it is located just above them.

The stability diagram obtained in this study shows that stability regions of DL surfaces lie well beyond the precipitation lines of TiO_2 and SrO oxides. Therefore, we expect that precipitation of strontium and titanium oxides will occur much earlier, before any of the studied DL terminations can form. This allows us also to suppose that the SrO or TiO_2 oxide films would grow preferably on SrTiO_3 perovskite

through cluster formation rather than in layer-by-layer mode. The (2×1) DL TiO_2 -terminated surface has a slightly lower free surface energy and thus is more stable than the unreconstructed DL TiO_2 -terminated $\text{SrTiO}_3(001)$ surface. Therefore, this reconstructed DL TiO_2 -terminated surface is more stable than the unreconstructed one. Overall, we find that within the range of SrTiO_3 stability, only regular SrO - and TiO_2 -terminated surfaces are stable. The stability region of the SrO -terminated (001) surface covers almost the entire region of SrTiO_3 stability. In contrast, a TiO_2 -terminated surface is stable only within a narrow stripe along the TiO_2 precipitation line. Our results lead also to the conclusion that Sr precipitation on the SrTiO_3 surface never occurs under equilibrium conditions. When oxygen gas partial pressure decreases at constant temperature, we expect either TiO_2 precipitation or Ti atom reduction with metallic particle formation. Increase of chemical potential of Sr atoms will lead to precipitation of SrO .

The analysis presented here assumes that all species are in thermodynamical equilibrium with all reservoirs, including oxygen atmosphere. In reality, the temperature dependencies of diffusion for various atoms are very different. The same is true for evaporation and condensation of different species at the surface and for defect creation. If thermodynamical equi-

librium is not reached, these kinetic processes will determine the surface structure, which, in particular, could turn out to be (2×1) DL TiO_2 -terminated surfaces as observed by Erdman *et al.*¹⁴

Application of the hybrid DFT Hartree-Fock functional allowed us to greatly improve the accuracy of our analysis with respect to pure DFT computations. We were able to obtain nearly perfect agreement of calculated and experimental formation energies and, therefore, to determine very well the stability boundaries of different crystals. We expect that the same high accuracy was achieved in determination of surface Gibbs free energies and regions of stability for the surface structures investigated in this study.

ACKNOWLEDGMENTS

The authors thank L. Marks, E. Spohr, R. Konings, and R. Caciuffo for stimulating discussions. This study was supported by the MRSEC program of the National Science Foundation (DMR-0076091). S.P. gratefully acknowledges also funding from the European Social Fund (ESF). This study was also partly supported by the Latvian Research programme on Functional Materials and Technologies for Microelectronics and Photonics (Project No. 05.0005.1.1).

*Electronic address: piskunov@lu.lv

¹C. Noguera, *Physics and Chemistry at Oxide Surfaces* (Cambridge University Press, New York, 1996).

²V. E. Henrich and P. A. Cox, *The Surface Science of Metal Oxides* (Cambridge University Press, New York, 1994).

³M. Kawasaki, K. Takahashi, T. Maeda, R. Tsuchiya, M. Shinohara, O. Ishiyama, T. Yonezawa, M. Yoshimoto, and H. Koinuma, *Science* **266**, 1540 (1994).

⁴T. Hikita, T. Hanada, M. Kudo, and M. Kawai, *Surf. Sci.* **287/288**, 377 (1993).

⁵A. Hirata, K. Saiki, A. Koma, and A. Ando, *Surf. Sci.* **319**, 267 (1994).

⁶A. G. Schrott, J. A. Misewich, M. Copel, D. W. Abraham, and Y. Zhang, *Appl. Phys. Lett.* **79**, 1786 (2002).

⁷T. Kubo and H. Nozoye, *Surf. Sci.* **542**, 177 (2003).

⁸K. Szot and W. Speier, *Phys. Rev. B* **60**, 5909 (1999).

⁹H. Wei, L. Beuermann, J. Helmbold, G. Borchardt, V. Kempter, G. Lilienkamp, and W. Maus-Friedrichs, *J. Eur. Ceram. Soc.* **21**, 1677 (2001).

¹⁰Y. Liang and D. A. Bonnell, *Surf. Sci.* **310**, 128 (1994).

¹¹M. Yoshimoto, T. Maeda, K. Shimozone, H. Koinuma, M. Shinohara, O. Ishiyama, and F. Ohtani, *Appl. Phys. Lett.* **65**, 3197 (1994).

¹²M. R. Castell, *Surf. Sci.* **505**, 1 (2002).

¹³T. Nishimura, A. Ikeda, H. Namba, T. Morishita, and Y. Kido, *Surf. Sci.* **421**, 273 (1999).

¹⁴N. Erdman, K. R. Poeppelmeier, M. Asta, O. Warschkow, D. E. Ellis, and L. D. Marks, *Nature (London)* **419**, 55 (2002).

¹⁵N. Erdman and L. D. Marks, *Surf. Sci.* **526**, 107 (2003).

¹⁶N. Erdman, O. Warschkow, M. Asta, K. R. Poeppelmeier, D. E. Ellis, and L. D. Marks, *J. Am. Chem. Soc.* **125**, 10050 (2003).

¹⁷M. S. Martín Gonzáles, M. H. Aguirre, E. Morán, M. Á. Alario-Franco, V. Perez-Dieste, J. Avila, and M. C. Asensio, *Solid State Sci.* **2**, 519 (2000).

¹⁸A. Kazimirov, D. M. Goodner, M. J. Bedzyk, J. Bai, and C. R. Hubbard, *Surf. Sci.* **492**, L711 (2001).

¹⁹S. B. Lee, F. Phillipp, W. Sigle, and M. Rühle, *Ultramicroscopy* **104**, 30 (2005).

²⁰F. Silly and M. R. Castell, *Appl. Phys. Lett.* **85**, 3223 (2004).

²¹A. Gunhold, L. Beuermann, M. Frerichs, V. Kempter, K. Gömann, G. Borchardt, and W. Maus-Friedrichs, *Surf. Sci.* **523**, 80 (2003).

²²*Ferroelectrics and Related Substances*, edited by K. H. Hellwege and A. M. Hellwege, Landolt-Bornstein, New Series, Group III, Vol. 3 (Springer-Verlag, Berlin, 1969).

²³P. W. Tasker, *J. Phys. C* **12**, 4977 (1979).

²⁴J. Padilla and D. Vanderbilt, *Surf. Sci.* **418**, 64 (1998).

²⁵E. Heifets, E. A. Kotomin, and J. Maier, *Surf. Sci.* **462**, 19 (2000).

²⁶S. Piskunov, E. A. Kotomin, E. Heifets, J. Maier, R. I. Eglitis, and G. Borstel, *Surf. Sci.* **575**, 75 (2005).

²⁷J. A. Misewich and A. G. Schrott, *Appl. Phys. Lett.* **76**, 3632 (2000).

²⁸J. M. Huijbregtse, J. H. Rector, and B. Dam, *Physica C* **351**, 183 (2001).

²⁹G.-X. Qian, R. M. Martin, and D. J. Chadi, *Phys. Rev. B* **38**, 7649 (1988).

³⁰J. Padilla and D. Vanderbilt, *Phys. Rev. B* **56**, 1625 (1997).

³¹A. Pojani, F. Finocchi, and C. Noguera, *Surf. Sci.* **442**, 179 (1999).

³²F. Bottin, F. Finocchi, and C. Noguera, *Phys. Rev. B* **68**, 035418 (2003).

- ³³K. Reuter and M. Scheffler, Phys. Rev. B **65**, 035406 (2001).
- ³⁴K. Johnston, M. R. Castell, A. T. Paxton, and M. W. Finnis, Phys. Rev. B **70**, 085415 (2004).
- ³⁵L. M. Liborio, C. G. Sánchez, A. T. Paxton, and M. W. Finnis, J. Phys.: Condens. Matter **17**, L223 (2005).
- ³⁶A. D. Becke, J. Chem. Phys. **98**, 5648 (1993).
- ³⁷V. R. Saunders, R. Dovesi, C. Roetti, R. Orlando, C. M. Zicovich-Wilson, N. M. Harrison, K. Doll, B. Civalleri, I. J. Bush, Ph. D'Arco, and M. Llunell, *CRYSTAL2003 User's Manual* (Università di Torino, Torino, 2003), <http://www.crystal.unito.it/>
- ³⁸S. Piskunov, E. Heifets, R. I. Eglitis, and G. Borstel, Comput. Mater. Sci. **29**, 165 (2004).
- ³⁹P. J. Hay and W. R. Wadt, J. Chem. Phys. **82**, 299 (1984).
- ⁴⁰D. Muñoz, N. M. Harrison, and F. Illas, Phys. Rev. B **69**, 085115 (2004).
- ⁴¹J. Carrasco, F. Illas, N. Lopez, E. A. Kotomin, Y. F. Zhukovskii, R. A. Evarestov, Y. A. Mastrikov, S. Piskunov, and J. Maier, Phys. Rev. B **73**, 064106 (2006).
- ⁴²H. J. Monkhorst and J. D. Pack, Phys. Rev. B **13**, 5188 (1976).
- ⁴³E. Heifets, J. Ho, and B. Merinov, Phys. Rev. B (to be published).
- ⁴⁴M. W. Chase, *NIST-JANAF Thermochemical Tables*, 4th ed. (American Chemical Society, American Institute of Physics for the National Institute of Standards and Technology, Washington, DC, New York, 1998).
- ⁴⁵L. B. Pankratz, *Thermodynamic Properties of Carbides, Nitrides, and Other Selected Substances* (United States Department of the Interior, Bureau of Mines, Washington, DC, 1995).
- ⁴⁶K. van Benthem, C. Elsässer, and R. H. French, J. Appl. Phys. **90**, 6156 (2001).
- ⁴⁷X. D. Zhu, Y. Y. Fei, H. B. Lu, and G. Z. Yang, Appl. Phys. Lett. **87**, 051903 (2005).
- ⁴⁸C. Argirusis, S. Wagner, W. Menesklou, C. Warnke, T. Damjanovic, G. Borchardt, and E. Ivers-Tiffée, Phys. Chem. Chem. Phys. **7**, 3523 (2005).